Multiplex stimulated Raman imaging with white probe-light from a photonic-crystal fibre and with multi-wavelength balanced detection

2014 J. Phys. D: Appl. Phys. 47 345401

(http://iopscience.iop.org/0022-3727/47/34/345401)

IOP Publishing Journal of Physics D: Applied Physics
J. Phys. D: Appl. Phys. **47** (2014) 345401 (9pp) doi:10.1088/0022-3727/47/34/345401

Multiplex stimulated Raman imaging with white probe-light from a photonic-crystal fibre and with multi-wavelength balanced detection

K Seto[1,2], Y Okuda[3], E Tokunaga[3] and T Kobayashi[1,2,4,5]

[1] Advanced Ultrafast Laser Research Center, The University of Electro-Communications, 1-5-1, Chofugaoka, Chofu, Tokyo 182-8585, Japan
[2] CREST, Japan Science and Technology Agency, 4-1-8, Honcho, Kawaguchi, Saitama 332-0012, Japan
[3] Department of Physics, Faculty of Science, Tokyo University of Science, 1-3 Kagurazaka, Shinjuku-ku, Tokyo, 162-8601, Japan
[4] Department of Electrophysics, National Chiao-Tung University, Hsinchu 300, Taiwan
[5] Institute of Laser Engineering, Osaka University, 2-6 Yamada-oka, Suita, Osaka 565-0971, Japan

E-mail: kobayashi@ils.uec.ac.jp

Received 16 May 2014, revised 21 June 2014
Accepted for publication 26 June 2014
Published 5 August 2014

Abstract
A straightforward method for spectral stimulated Raman scattering (SRS) microscopy is to measure the scanned gain/loss spectrum of a white probe light from a photonic crystal fibre (PCF). However, the intensity of the white light noise is a serious problem for SRS microscopy. In this study, we have demonstrated simultaneous two-wavelength SRS microscopy with PCF through balanced detection suitable for spectroscopy with a modification of an auto-balance scheme. The developed auto-balance detection system suppresses the degradation of noise cancellation performance caused by a sample, and is suitable for spectral SRS imaging with simple and robust optics.

Keywords: stimulated Raman, noise cancellation, microscopy

(Some figures may appear in colour only in the online journal)

S Online supplementary data available from stacks.iop.org/JPhysD/47/345401/mmedia

1. Introduction

Recently, stimulated Raman scattering (SRS) microscopy has been studied as one of the promising tool for high speed no-labelling chemical imaging of a biological sample, based on molecular vibration [1–5]. As the high speed chemical imaging method, coherent anti-Stokes Raman scattering (CARS) microscopy has also been extensively studied [6–12]. However, a CARS signal contains a non-resonant background (NBR) component, and this NBR generates an artificial image and spectral distortion. Additionally, the signal intensity is proportional to the square of a molecular concentration, and results in the degradation of its identification ability and quantitative capacity. Various methods have been developed to solve these problems [11, 12]. SRS microscopy is advantageous over CARS microscopy, since an SRS signal does not contain an NBR signal, and the signal intensity is proportional to the concentration. With these advantages, the imaging based on a Raman band in the finger print region [5] and quantitative analysis without data processing has been demonstrated [13].

In SRS microscopy, at least two pulsed beams with different wavenumbers are irradiated on the sample. When the difference between these wavenumbers is equal to a molecular vibration wavenumber, a photon of the pump beam is annihilated and that of the Stokes beam is created. Thus, through adjusting the difference to the target molecular vibration and observing the intensity of the pump or Stokes beam, the chemical image on this vibration is obtained by scanning the beams or sample. However, since this intensity modulation depth is typically of the order of 10^{-4}, the intensity noise of the light source is a serious problem. Usually for

SRS microscopy, to reject light intensity noise and enhance the signal to noise ratio (SNR), the intensity of the pump or Stokes beam is modulated and the counterpart is lock-in detected at the modulation frequency [1, 14, 15].

In commonly used lock-in detection, a single wavelength probe beam is detected. One of the recent trends of study is to then develop a method to observe a distribution of more than one substance at one shot imaging and a method for spectral imaging. Although various methods for spectral imaging and multi-element imaging have been developed [3, 13, 16–21], they require complicated optics and adjustment, or only a few spectral components are observed. Previously, we developed a simple method with a white probe beam from a photonic crystal fibre (PCF) [22–24] and multi-wavelength lock-in detection with a multi-channel lock-in amplifier (MLA) through a spectrometer [25]. In this method, a common laser oscillator is used to prepare both the white probe and the monochromatic pump beams, and hence the probe and pump are automatically synchronized, resulting in a simple and robust system. However, the intensity noise of the white light is so prominent in a broad frequency range [26–28] that it is difficult to achieve high speed imaging with high SNR, even using the lock-in detection.

The intensity noise of the probe beam can be cancelled by a balanced detection method [29–33]. In this method, the light source is split into probe and reference beams, and after measurement of a sample with the probe, the signal is obtained as a difference between the probe and reference signals. Here, the light intensity noise of the probe beam is the product of the intensity fluctuation of the white light source and the fluctuation of the splitting ratio into the probe and reference beams due to the nature of the particle of the photon. The fluctuation of the white light source causes common intensity fluctuations between the probe and reference beams, and hence this fluctuation is cancelled through the balanced detection. The fluctuation of the splitting ratio results in independent intensity fluctuations between the probe and reference beams, and thus, the noise intensity caused by this effect cannot be cancelled by the balanced detection. Hereafter, we define the intensity fluctuation originated in the light source as 'light intensity noise', whereas we define the fluctuation originated in the splitting-ratio fluctuation due to the particle nature of the photon as 'shot noise'. The SNR limit of this detection is determined by the sum of the shot noises of the probe and reference beams. To apply balanced detection to the multi-wavelength detection for spectral imaging, at least the following three requirements must be fulfiled. Firstly, the probe and reference beams are spectrally dispersed and detected in an exactly the same bandwidth, since intensity fluctuations are completely different for different wavelengths. Secondly, signal gains for the beams are adjusted independently for each corresponding wavelength, since the splitting ratio is different for each wavelength due to wavelength dependencies of the practical optics. Without this adjustment, when the optical intensity ratio is balanced at a particular wavelength, those at the other wavelengths are unbalanced. Finally, the unbalance caused by reflection, scattering, and absorption by the sample is to be corrected during an imaging process. The first requirement can be fulfiled by using a common photodetector for the probe and reference beams [30, 32]. This makes it possible to use a common spectrometer for the beams, and the spectral condition is automatically unified. The method to fulfil the second requirement has been developed in our previous study [32]. The detail of this method is mentioned later, and in this study, automatical adjustment (auto-balance) has been developed for a practical application of this method. The final requirement is assumed to be fulfiled with the irradiation of the beams at the same position of the sample, and detection by the common photodetector [30, 32], called collinear balanced detection (CBD). Through the same optical path, the intensity modulations by the sample are assumed to be common. However, we have found that in a practical application, the balance is displaced even with the CBD. In this study, we point out this problem and report the developed auto-balance scheme that is also helpful to solve this problem. Although the idea of auto-balance is well known [31, 33], usually the beams are detected by different photodetectors, and hence it is difficult to fulfil the first requirement. Based on our method, we demonstrate simultaneous two-wavelength SRS imaging on simple optics with the PCF, in preparation for practical high speed spectral SRS imaging.

2. Methods

2.1. Stimulated Raman microscope

Figure 1 illustrates the schematic of the experimental setup. A titanium–sapphire laser oscillator (Mira 900 P, COHERENT) generates 2.5 ps duration pulsed light of 76.3 MHz repetition cycle at 800 nm. The average output power is 600 mW. The pulse is split into two; one is used for white-light generation, and the other is for a pump beam.

The former pulse is coupled into a 1 m length PCF of the zero-dispersion wavelength of 790 nm (NL-2.3-790-2, THORLABS) by a microscope objective ($\times$ 40, numerical aperture (NA) $=$ 0.65) through a half-wave plate, and is then converted to the white-light continuum. This half-wave plate is for adjustment of the polarization of the input pulse, to maximize the efficiency of the continuum generation; the efficiency is found to be dependent on the polarization angle due to a small fraction of birefringence of this fibre. The white light output is collimated by a microscope objective ($\times$40, NA $=$ 0.65), and its polarization angle is adjusted by a Glan–Thompson prism polarizer; the splitting ratio into the probe and reference beams is adjusted by this polarization angle. The generated continuum pulse beam is split into the probe and reference beams (shown as the orange and green lines, respectively) by a broad band polarizing beam splitter (PBS) (CM1-PBS252, THORLABS). The reference beam is delayed by a quarter cycle of the pulse repetition by an additional 98 cm optical path, and spatially overlapped on the probe beam in a PBS. The alignment for the spatial overlap is checked with an alignment scope (TEL300-38, TRIOPPTICS) with a 3.5 arcsec accuracy to confirm that the probe and reference beams pass the same position of a sample.

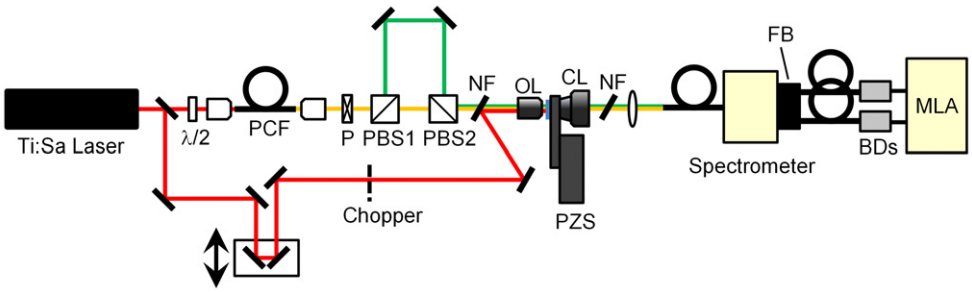

Figure 1. Schematic of the SRS microscope with multi-wavelength balanced detection. The red, orange, and green lines are the 800 nm pulse beam, white probe and reference pulses, respectively. λ/2: half-wave plate; PCF: photonic crystal fibre; P: Glan–Thompson polarizer; PBS1 and PBS2: polarizing beam splitters; NF: notch filter; OL: microscope objective; CL: condenser lens; PZS: piezo stage; FB: 16 × 128 fibre bundle; BD: the developed balanced detector; MLA: multi-channel lock-in amplifier.

Spectral components around 800 nm in the probe and reference beams are rejected by a notch filter (NF808-34, THORLABS).

The latter 800 nm pulse for pump beam is sent to a delay stage to be temporally overlapped with the probe pulse. Then the beam is chopped at 4.48 kHz, and spatially overlapped and collinearly aligned with the probe beam on the notch filter.

The three beams are tightly focused on the sample by a microscope objective ($\times 40$, NA $= 0.85$). The sample is scanned by a piezo actuator on a stage (NanoMax300, THORLABS), and an SRS image is captured. The light transmitted through the sample is collected by a condenser lens (NA $= 1.4$). After the pump beam (component of 800 nm) is rejected by a notch filter (NF808-34, THORLABS), the probe and reference beams are guided into a spectrometer (SpectraPro-300i, ACTON) by a multi-mode optical fibre. Thus, the probe and reference beams are spectrally dispersed by the common spectrometer. The focal length and F number of the spectrometer are 30 cm and 4, respectively. The groove number, blaze wavelength, and line dispersion of the grating are 300 g mm^{-1}, 500 nm, and 10.8 nm mm^{-1}, respectively. The spectrally dispersed beams are imaged on the entrance facet of a 16 × 128 fibre (core/clad: 100/110 μm) bundle. The spectrum on the facet is split into 128 wavelengths, and each of the sixteen fibres are bundled. In this study, two components of the wavelength are simultaneously observed by two balanced detectors. The outputs are simultaneously measured with a multi-channel lock-in amplifier (Model 7210, SIGNAL RECOVERY).

2.2. Balanced detector

The developed balanced detector is based on the scheme described in our previous study [32]. Figure 2 shows the block diagram of the balanced detector.

A common spectral component of the probe and reference beams from the common spectrometer is guided by the sixteen bundled fibres into a common avalanche photodiode (APD) (S5343, HAMAMATSU). The optical current signal is converted to a voltage signal by a resonator of the resonant frequency at 76.3 MHz. This resonator is composed of a coil and a capacitor, and hence free of thermal noise. The signals of the probe and reference beams are expressed as $Aa\,(1+m)\cos(\omega t)$ and $Ab\sin(\omega t)$, respectively, with the phase relation

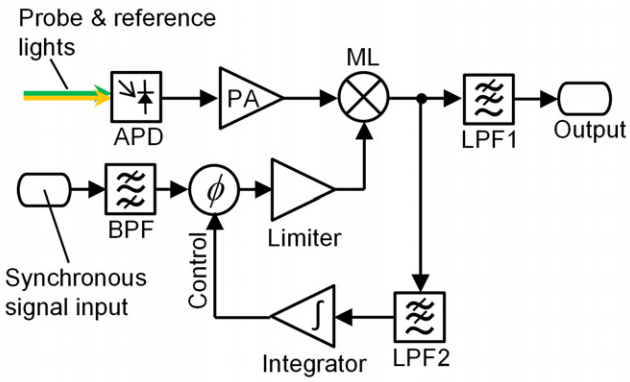

Figure 2. The block diagram of a balanced detector for spectral imaging with a feed-back loop for auto-balanced detection. APD: avalanche photodiode; PA: pre-amplifier; ML: multiplier; BPF: band-pass filter; LPF1: low-pass filter to reject RF signal; LPF2: low-pass filter to reject RF and SRS signals.

due to the quarter cycle optical delay of the reference beam. Here, A, a, b, m, and ω are the intensity of the white pulse, splitting ratios ($a + b = 1$), modulation by the SRS, and the repetition frequency of the pulse source, respectively. Thus, the voltage signal from the resonator is the sum of the signals expressed by

$$A\left\{a\,(1+m)\cos(\omega t) + b\sin(\omega t)\right\}. \tag{1}$$

This signal is amplified by a pre-amplifier (PA) and transferred to a multiplier (ML).

Also, a synchronous signal of the light source is prepared by observing the optical pulse with a photodetector. The fundamental component of the synchronous pulse is extracted thorough a band-pass filter (BPF). The phase (δ) of this signal is adjusted by a phase sifter, and the amplitude (D) is fixed by a limiter. This signal is expressed as $D\cos(\omega t + \delta)$. Then, the voltage signal of the probe and reference beams is multiplied by this synchronous signal in the ML. The multiplied result is proportional to

$$AD\Big[a\,(1+m)\left\{\cos(2\omega t+\delta)+\cos\delta\right\} + b\left\{\sin(2\omega t+\delta)-\sin\delta\right\}\Big]. \tag{2}$$

The high frequency (radio frequency (RF)) components in equation (2) are removed by a low-pass filter (LPF1), and the output signal is proportional to

$$A\{a(1+m)\cos\delta - b\sin\delta\}. \quad (3)$$

Therefore, the output is the difference between the probe and reference signals. Note that these signal gains are adjusted by the δ. By setting the δ as $\tan^{-1}(a/b) + 2n\pi$, the carrier signal of $Aa\cos\delta$ is subtracted and the only modulation signal is output as $(Aa\cos\delta)m$. A phase error due to displacement of the optical delay of the reference beam effectively results in an alternation of the splitting ratio, and thus the complete cancellation of the carrier is still possible (appendix A). When the balanced detection is not applied, the output signal amplitude is proportional to $A+Am$. Thus, a small modulation (m) (typically 10^{-4} order) on the large carrier signal (A) should be detected. This is problematic, especially when the amplitude of the carrier is strongly fluctuating as in the case of the white-continuum light.

When the δ is not adjusted, as the carrier signal is completely subtracted and/or the ratio of a and b are disturbed during imaging, the direct-current (dc) component appears in the output. As in this diagram, the value of δ is controlled by a feed-back mechanism based on the integrated signal of the dc component so that the dc component is zero (the integral control). The disturbances of a and b are thus corrected by this feed-back control. The response time of this feed-back should be set shorter than the dwelling time at one pixel in the imaging process, and appropriately longer than the modulation cycle of the Raman signal. If the response time is longer than the dwelling time, the feed-back control cannot respond to the disturbance during the imaging. Also, if the response time is shorter than the modulation cycle, the modulation signal is also feed-backed so that the signal is vanished.

By insertion of the LPF2 in the feed-back loop, the response speed can be increased through the adequate rejection of the modulation signal. However, the phase retardation of the loop at the cutoff frequency must be carefully checked. The phase retardation of an integrator is 90° at any frequency, and hence feed-back is always stable without LPF2. The LPF2 adds the retardation, and if the total retardation exceeds 180° at the cutoff frequency, the feed-back results in catastrophe due to the positive feed-back of the dc component. Additionally, the phase shifter and ML effectively change the gain of the control. Therefore, in setting the integration time, the gain and phase retardation of the LPF2, the gain in the ML (dependent on the δ), and the gain of the δ in the phase shifter against the control signal must be counted. The detailed scheme is described in appendix B, and concrete responses of the components depend on the electrical circuit. The concrete responses are described with the circuit diagram in the online supplemental information (stacks.iop.org/JPhysD/47/345401/mmedia).

3. Experiment

3.1. Noise cancellation performance

The noise cancellation performance was initially measured in the case without a sample. The light intensity was adjusted by a neutral-density (ND) filter so as not to saturate the detector. The signal of the light intensity noise was measured 140 times with the lock-in detection of the time constant of 10 ms. The dwelling time was set at 30 ms. The modulation equivalent noise density was evaluated as a tenth of the root-mean-square of these 140 data, normalized by the probe signal intensity. The value of δ was adjusted and fixed by an extra phase shifter so that output signals of the chopped probe and reference were equalized with the same optical input power. In measurements of the signal intensity of the probe (reference) beam, the auto-balance was turned off and the light was chopped with blocking the reference (probe) beam.

The probe beam noise was measured with turning off the feed-back, without chopping the light, and with blocking of the reference beam. The fixed balance detected noise was evaluated with inputting the reference light, and then the auto-balance detected noise was measured with turning on the feed-back. These evaluations were repeated in various intensity balances between the probe and reference by adjusting the polarizer. The probe light intensities were measured at the corresponding optical balances for the normalization factor of the modulation equivalent noise density, except for the auto-balanced case. For the auto-balanced case, the probe light intensity of the optically balanced case ($a = b$) was used for the normalization factor, since the gain for the probe beam was automatically controlled to the optically balanced case.

3.2. Two-colour SRS imaging

A sample made up of 4 μm polystyrene (PS) beads embedded in a polyvinyl alcohol (PVA) film on a glass slide was prepared. The observed Raman shifts were selected as the peaks of Raman bands of PS (3054 cm^{-1}) and PVA (2914 cm^{-1}). The optical balance was set at 3054 cm^{-1} by the polarizer, and the δs were adjusted so that the probe and reference signals were equated in respective of wavelength. The images were captured in three cases; without the reference beam and without the auto-balance, with the reference beam and without the auto-balance, and with the reference and with the auto-balance. Also, to investigate the disturbance of the optical balance by the sample, both the probe and reference beams were directly chopped and irradiated on the sample without the pump beam.

4. Results and discussion

4.1. Noise cancellation performance

Figure 3(a) shows the spectra of the probe and reference beams after the microscope. The white continuum contains 600–850 nm components, and covers whole Raman shifts of molecular vibrations. The dip around 800 nm is due to the spectral rejection by the notch filters. Figure 3(b) shows spectral unbalance of (probe–reference)/probe, and it is found that the unbalance fluctuated within 10% depending on the wavelength. This is due to the unbalance of optics for the probe and reference beams, and should be corrected for each wavelength for the multi-wavelength balanced detection. The balanced detector in this paper can correct this unbalance.

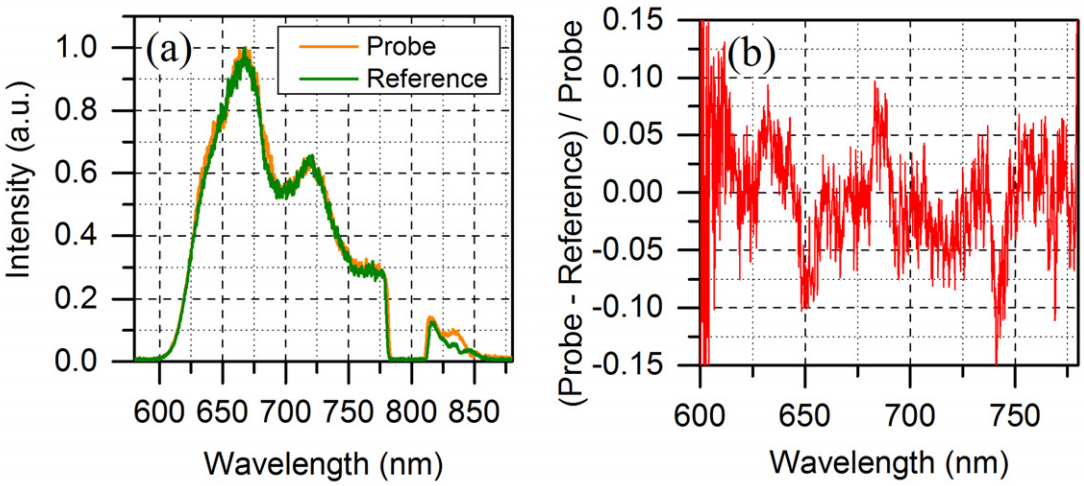

Figure 3. Spectra of probe and reference beams (a), intensity unbalance at the microscope (b).

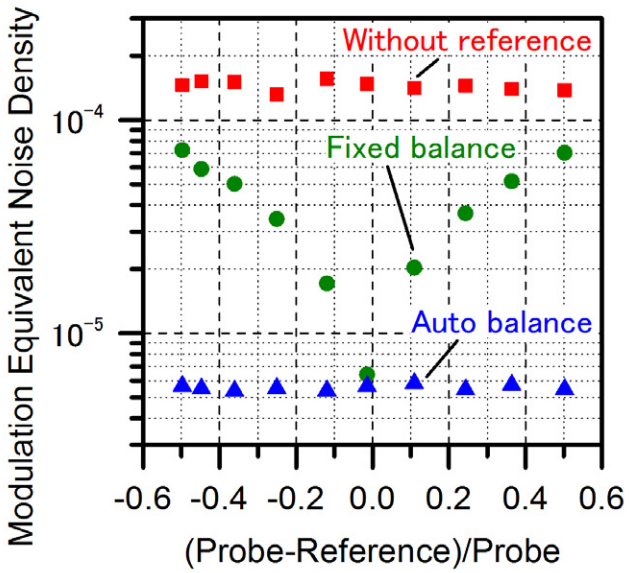

Figure 4. Noise cancellation performance and effect of the auto-balanced detection against the displacement of the optical unbalance between the probe and reference lights.

The modulation equivalent noise against various optical unbalance, (probe–reference)/probe is depicted in figure 4. The optical input power of the probe and reference beams at the APD is 6 μW. The noise density of the probe light (the red square plots) is $\sim 1.5 \times 10^{-4}\,\mathrm{Hz}^{-1/2}$. In the fixed-balanced case (the green round plots), the noise is $5.6 \times 10^{-6}\,\mathrm{Hz}^{-1/2}$ in the optically best balanced case, and thus 28 dB cancellation is achieved. However, when the optical unbalance is increased in both directions of probe > reference, or probe < reference, the noise proportionally increases due to imperfect subtraction. This is caused by the above mentioned unbalance of optics, long term instabilities of the optics, and/or the inhomogeneous nature of a sample (see the later discussion). In the auto-balanced case (blue triangle plots), the values of the noise are independent of the optical unbalance and they are almost the same as the value of the optically balanced case in the fixed-balanced case. This is due to the automatic correction of the unbalance, and thus the residual noise caused by the optical unbalance is completely cancelled out. It is found that the above mentioned feed-back successfully functions for noise cancellation.

However, SNR is affected by the splitting ratio since the gain for the SRS signal is dependent on the ratio, whereas the noise is independent of it. In equation (3), the signal intensity is proportional to $Aam\cos\delta$, where $\cos\delta$ is set as $b/(a^2+b^2)^{1/2}$ for the noise cancellation. SNR is dependent on the splitting ratio, as follows,

$$\mathrm{SNR} \propto \frac{ab}{\left(a^2+b^2\right)^{1/2}}. \tag{4}$$

From equation (4), it is found that SNR is maximized when $a = b$. Therefore, the condition of as equal splitting as possible is desirable for imaging, although the noise is cancelled at maximum efficiency at any splitting ratio.

4.2. Two-colour SRS imaging

Spontaneous Raman spectra of PS and PVA are shown in figure 5(a). A Raman band of PS assigned to CH stretching mode of the benzene ring and that of PVA assigned to CH stretching mode of the methylene groups are observed at 3054 and 2914 cm^{-1} Raman shifts, respectively. The SRS images of the sample are shown in figures 5(b)–(f). These images were captured with the time constant of 30 ms, and dwelling time of 60 ms. The pixel size is 0.25 $\times$ 0.25 μm, and image size is 41 $\times$ 41pixels. The images are illustrated in a unified rainbow colour scale. The reddish colour represents the stronger signal, and the purplish colour represents the weaker signal. The white colour represents a strong signal out-of-range of the scale.

Figures 5(b) and (c) are the SRS images captured on the 3054 and 2914 cm^{-1} Raman bands, respectively, with the fixed balance detection. In image (b), $\sim$4 μm discoid distribution of strong signal is captured, corresponding to the PS bead. In (c), the strong signal distribution is opposite to (b), due to the homogeneous distribution of PVA with the discoid

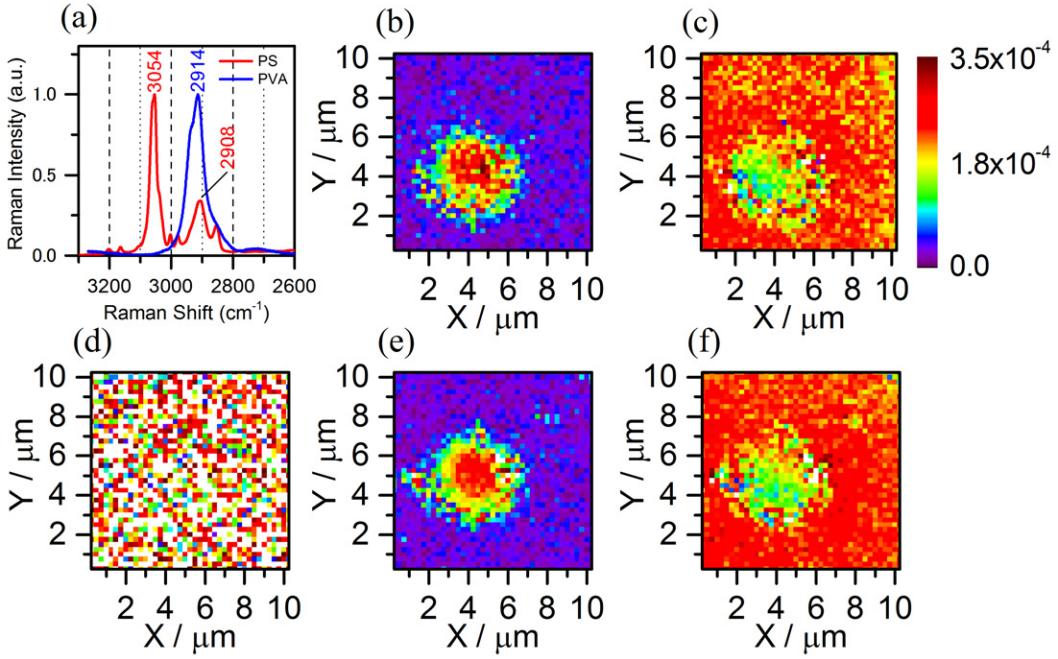

Figure 5. Spontaneous Raman spectra of PS and PVA (a), and SRS images of a 4 μm PS bead in PVA film (b)–(f). (b) and (c) SRS images captured with 3054 and 2914 cm^{-1} Raman bands through fixed-balanced detection, respectively. (d) SRS image with 3054 cm^{-1} without reference beam. (e) and (f) SRS images with 3054 and 2914 cm^{-1} Raman shifts through auto-balanced detection, respectively.

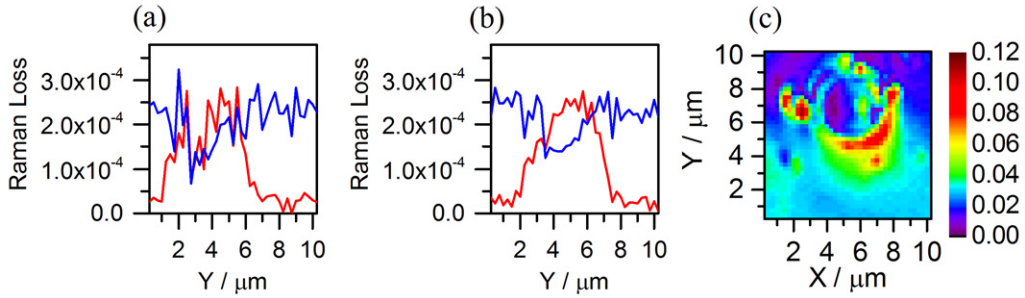

Figure 6. Cross-sectional intensity distributions of SRS images and optical unbalance caused by a sample. (a) Cross-sectional intensity distributions of the fixed-balanced case (figures 5(b) and (c)) on the $X = 4.25\,\mu$m lines. The blue and red lines represent the signal intensities of 3054 and 2914 cm^{-1} Raman bands, respectively. (b) Those of the auto-balanced case (figures 5(e) and (f)). (c) The image captured on the chopped probe and reference beams through fixed-balanced detection, normalized by the probe signal intensity.

exclusion by the PS bead. Image (d) is captured on 3054 cm^{-1} Raman shifts with blocking reference light. In this image, the SRS signal is buried in the light intensity noise of the probe light, and no structure is observed. The situation is the same as the image captured on 2914 cm^{-1} Raman shifts (not shown). Therefore, two-colour SRS imaging with the multi-wavelength balanced detection through a spectrometer is attained. Through increasing the number of channels, spectral SRS imaging of the simultaneous detection of the Raman shifts is readily realized.

The images (e) and (f) are captured on 3054 and 2914 cm^{-1} Raman bands, respectively, with the auto-balanced scheme. The contrasts of them are correspondingly similar to (b) and (c). These results indicate that light intensity noise is cancelled, while the SRS modulation signals are successfully obtained without being vanished during the imaging. The functionality of the scheme to design the parameters of the LPF2 and integrator in the feed-back loop is verified. Note that the SNR is better especially around the PS bead than that without the auto-balance.

Figures 6(a) and (b) are the cross-sections along the $X = 4.25\,\mu$m lines on the images of the fixed- and auto-balanced cases, respectively. In the fixed-balanced case, the signal of the 3054 cm^{-1} Raman band is strong, and that of the 2914 cm^{-1} band is dipped on the PS bead region. However, the signals are strongly fluctuated on this region despite the sphere shape of the bead. In the auto-balanced case, this fluctuation is suppressed. The cause of this fluctuation is explained by the disturbance of the optical balance between the probe and reference beams during imaging, as follows. Figure 6(c) is captured by directly chopped probe and reference beams through the fixed-balanced detection, and is normalized by the probe signal intensity. If the optical balance is maintained during the imaging, as assumed in the CBD, the value is zero or at least constant at any positions. However, for this sample, the value is upraised to 0.12, especially around the bead. This result clearly indicates the disturbance, and as a result, the light

noise of the probe is insufficiently or overly subtracted. In the auto-balanced case, the unbalance caused by this disturbance is corrected, and the light noise is well cancelled.

This disturbance is caused by at least three possible factors. One is imperfect alignment, although it is confirmed by the alignment telescope; the same optical path requires significantly severe alignment, and it is susceptible to mechanical displacement, especially in microscopy. Another one is the difference in the transmittance between the probe and reference against the inclined interface of different refractive indices. The probe and reference beams are prepared with the PBSs to maintain high throughput of the optics, and thus the polarization is perpendicular to each other. Thus, the reflectivity on the inclined interface differs in the beams. The last one is birefringence and dichroic nature of a sample. In our sample, unbalance is about 10%, and it reduces the cancellation to ∼20 dB. Additionally, this disturbance depends on the sample and position; this distribution may cause an artificial image. These introduce serious errors, especially in applications using a light source of large intensity noise such as the white light continuum. The auto-balanced scheme is required not only to make the system robust and to apply to spectral imaging, but also to eliminate the disturbance induced by the samples.

The contrast of the image of the 2914 cm^{-1} Raman band is lower than that of the 3054 cm^{-1} band. This is due to the overlap of the 2908 cm^{-1} band of PS on the 2914 cm^{-1} band of PVA (figure 5(*a*)). The ratio between the band areas of the 3054 and 2908 cm^{-1} bands in the spontaneous Raman spectrum is 1 : 0.68 with fitting of the Voigt function. Equally, the average signal intensity in the range of $Y = 4$–$5\,\mu$m of figure 6(*b*) of the 3054 and 2914 cm^{-1} bands are 2.34×10^{-4} and 1.45×10^{-4}, respectively. The signal intensity ratio is 1 : 0.61, and is close to the band-area ratio. Therefore, the dominant origin of the signal on the PS bead in figures 5(*c*) and (*f*) is estimated as not the 2914 cm^{-1} band of PVA film but the 2904 cm^{-1} band of the PS bead.

In this study, and also for the auto-balanced detection, both the probe and the reference beams are transmitted through the same position of the sample to compare it with that of the fixed-balanced scheme. However, this configuration is redundant for practical auto-balance detection; the reference beam is not required to pass through the sample, and can bypass the microscope and be overlapped on the probe beam before the spectrometer. By this bypassed configuration, the risk of sample degradation by the reference beam is reduced.

5. Conclusion

Simultaneous two-colour SRS imaging with the picosecond continuum probe light is realized through the balanced detector for a multi-wavelength measurement. The probe and reference beams are detected by a common photodetector, and thus this balanced detection is readily applicable to spectroscopy. Additionally, an auto-balance scheme is developed for this balanced detection for a practical multi-wavelength observation and an imaging application. In this scheme, the phase of the synchronous signal, which determines the gains for the probe and reference signal, is successfully feed-back controlled. There is limited effectiveness in the case of the method of setting the same optical path for the probe and reference beams through a sample to maintain optical balance during imaging. This limitation is especially serious for an application with the noisy white-continuum probe beam. This problem is well overcome by the developed auto-balance scheme with appropriate setting of the feed-back response.

In this SRS microscopy, a single light source is used through preparing a white-continuum probe beam by a PCF. The system does not require synchronization of plural light sources or scanning wavelength of the light, and thus the optics are simple and robust. Although the number of observed wavelengths is two in the present study, spectral imaging by multi-wavelength observation is readily realized through increasing the number of observation wavelengths. Based on this study, high speed spectral SRS imaging is readily realized with high temporal coincidence in respective Raman shifts.

Acknowledgments

This study was partially supported by a joint research project at the Institute of Laser Engineering, Osaka University, under contract number B1-27. This work was partially supported by JSPS KAKENHI Grant-in-Aid for Challenging Exploratory Research of contract number 26620117.

Appendix A

A phase error (δ_e) of the reference beam from the quarter cycle of the pulse repetition effectively causes an alternation of the splitting ratio, as follows. The signal from the resonator is (equation (1) containing δ_e),

$$A\left\{a\left(1+m\right)\cos\left(\omega t\right)+b\sin\left(\omega t+\delta_e\right)\right\}. \tag{A1}$$

This is rewritten as

$$A\left\{a'\left(1+m'\right)\cos\left(\omega t\right)+b'\sin\left(\omega t\right)\right\}. \tag{A2}$$

Here,

$$a' = a + b\sin\delta_e, \tag{A3}$$

$$b' = b\cos\delta_e, \tag{A4}$$

$$m' = \frac{a}{a+b\sin\delta_e}m. \tag{A5}$$

Equation (A2) is effectively the same as equation (1). Therefore, the light intensity noise can still be completely cancelled through the adjustment of the phase of the synchronous signal as $\tan^{-1}(a'/b') + 2n\pi$.

Appendix B

The system diagram of the feed-back loop is illustrated in figure B1. In this case, a controlled object P and detector D are the ML and LPF2, respectively, and controller C is composed of the integrator and phase shifter.

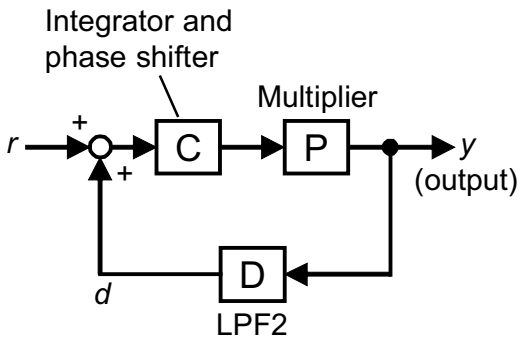

Figure B1. System diagram for feed-back loop. C: controller (integrator and phase shifter in this study); P: controlled object (multiplier); D: detector (LPF2).

The d and r indicate the dc component in the output and the target value of the dc component. In this study, the r is set as zero. The value of d for the close loop response is given by

$$d = \frac{\mathrm{DPC}}{1 - \mathrm{DPC}} r. \tag{B1}$$

Here, the product of the response functions of D, P and C is the open-loop response function in which D and P are the responses of the LPF2 and ML, respectively, and C is the product of the responses of the integrator and phase shifter. Note, the values of the responses are different in dimensions. The output of the phase shifter is phase, δ, and input is the voltage from the integrator, V_i. Thus, the C including the integrator is expressed as

$$\mathrm{C} = \frac{\mathrm{d}\delta}{\mathrm{d}V_i} \frac{1}{T_i \mathrm{i}\omega}. \tag{B2}$$

The latter term is the response of the integrator. The response of P against δ is

$$\mathrm{P} = \frac{\mathrm{d}\,(y\,(\mathrm{i}\omega))}{\mathrm{d}\delta}. \tag{B3}$$

Here, $y(\mathrm{i}\omega)$ is the output of the balanced detector. Therefore, the open-loop response is expressed as follows

$$\mathrm{DPC} = \mathrm{D} \frac{\mathrm{d}\,y}{\mathrm{d}\delta} \frac{\mathrm{d}\delta}{\mathrm{d}V_i} \frac{1}{T_i \mathrm{i}\omega}. \tag{B4}$$

From equation (B1) and (B4), the sign of the DPC must be negative, and the phase retardation at the cutoff frequency (when $|\mathrm{DPC}| = 1$) must be less than 180° to make the feed-back loop stable. To avoid ringing, it is desirable that the retardation is less than 120° (or phase margin is more than 60°). The concrete response depends on the circuit, and is described in online supplemental information (stacks.iop.org/JPhysD/47/345401/mmedia).

References

[1] Freudiger C W, Min W, Saar B G, Lu S, Holtom G R, He C, Tsai J C, Kang J X and Xie X S 2008 Label-free biomedical imaging with high sensitivity by stimulated raman scattering microscopy *Science* **322** 1857–60

[2] Saar B G, Freudiger C W, Reichman J, Stanley C M, Holtom G R and Xie X S 2010 Video-rate molecular imaging *in vivo* with stimulated Raman scattering *Science* **330** 1368–70

[3] Ozeki Y, Umemura W, Otsuka Y, Satoh S, Hashimoto H, Sumimura K, Nishizawa N, Fukui K and Itoh K 2012 High-speed molecular spectral imaging of tissue with stimulated Raman scattering *Nature Photon.* **6** 845–51

[4] Ozeki Y and Itoh K 2010 Stimulated Raman scattering microscopy for live-cell imaging with high contrast and high sensitivity *Laser Phys.* **20** 1114–8

[5] Zhang X, Roeffaers M B J, Basu S, Daniele J R, Fu D, Freudiger C W, Holtom G R and Xie X S 2012 Label-free live-cell imaging of nucleic acids using stimulated Raman scattering microscopy *ChemPhysChem* **13** 1054–9

[6] Duncan M D, Reintjes J and Manuccia T J 1982 Scanning coherent anti-Stokes Raman microscope *Opt. Lett.* **7** 350–2

[7] Zumbusch A, Holtom G R and Xie X S 1999 Three-dimensional vibrational imaging by coherent anti-stokes Raman scattering *Phys. Rev. Lett.* **82** 4142–5

[8] Kee T W and Cicerone M T 2004 Simple approach to one-laser, broadband coherent anti-Stokes Raman scattering microscopy *Opt. Lett.* **29** 2701–3

[9] Evans C L, Potma E O, Puoris'haag M, Côté D, Lin C P and Xie X S 2005 Chemical imaging of tissue *in vivo* with video-rate coherent anti-Stokes Raman scattering microscopy *Proc. Natl Acad. Sci. USA* **102** 16807–12

[10] Lütgens M, Chatzipapadopoulos S and Lochbrunner S 2012 Coherent anti-Stokes Raman scattering with broadband excitation and narrowband probe *Opt. Express* **20** 6478–87

[11] Okuno M, Kano H, Leproux P, Couderc V, Day J P R, Bonn M and Hamaguchi H 2010 Quantitative CARS molecular fingerprinting of single living cells with the use of the maximum entropy method *Angew. Chem. Int. Edn* **49** 6773–7

[12] Suzuki T and Misawa K 2011 Efficient heterodyne CARS measurement by combining spectral phase modulation with temporal delay technique *Opt. Express* **19** 11463–70

[13] Fu D, Lu F-K, Zhang X, Freudiger C, Pernik D R, Holtom G and Xie X S 2012 Quantitative chemical imaging with multiplex stimulated Raman scattering microscopy *J. Am. Chem. Soc.* **134** 3623–6

[14] Ozeki Y, Kitagawa Y, Sumimura K, Nishizawa N, Umemura W, Kajiyama S i, Fukui K and Itoh K 2010 Stimulated Raman scattering microscope with shot noise limited sensitivity using subharmonically synchronized laser pulses *Opt. Express* **18** 13708–19

[15] Nandakumar P, Kovalev A and Volkmer A 2009 Vibrational imaging based on stimulated Raman scattering microscopy *New J. Phys.* **11** 1–9

[16] Lu F-K, Ji M, Fu D, Ni X, Freudiger C W, Holtom G and Xie X S 2012 Multicolor stimulated Raman scattering microscopy *Mol. Phys.* **110** 1927–32
[17] Fu D, Holtom G, Freudiger C, Zhang X and Xie X S 2012 Hyperspectral imaging with stimulated Raman scattering by chirped femtosecond lasers *J. Phys. Chem.* B **117** 4634–40
[18] Freudiger C W, Min W, Holtom G R, Xu B, Dantus M and Xie X S 2011 Highly specific label-free molecular imaging with spectrally tailored excitation-stimulated Raman scattering (STE-SRS) microscopy *Nature Photon.* **5** 103–9
[19] Ozeki Y, Umemura W, Sumimura K, Nishizawa N, Fukui K and Itoh K 2012 Stimulated Raman hyperspectral imaging based on spectral filtering of broadband fiber laser pulses *Opt. Lett.* **37** 431–3
[20] Andresen E R, Berto P and Rigneault H 2011 Stimulated Raman scattering microscopy by spectral focusing and fiber-generated soliton as Stokes pulse *Opt. Lett.* **36** 2387–9
[21] Beier H T, Noojin G D and Rockwell B A 2011 Stimulated Raman scattering using a single femtosecond oscillator with flexibility for imaging and spectral applications *Opt. Express* **19** 18885–92
[22] Dudley J M and Coen S 2006 Supercontinuum generation in photonic crystal fiber *Rev. Mod. Phys.* **78** 1135–84
[23] Husakou A V and Herrmann J 2001 Supercontinuum generation of higher-order solitons by fission in photonic crystal fibers *Phys. Rev. Lett.* **87** 203901
[24] Herrmann J, Griebner U, Zhavoronkov N, Husakou A, Nickel D, Knight J C, Wadsworth W J, Russell P S J and Korn G 2002 Experimental evidence for supercontinuum generation by fission of higher-order solitons in photonic fibers *Phys. Rev. Lett.* **88** 173901
[25] Seto K, Okuda Y, Tokunaga E and Kobayashi T 2013 Development of a multiplex stimulated Raman microscope for spectral imaging through multi-channel lock-in detection *Rev. Sci. Instrum.* **84** 083705
[26] Corwin K L, Newbury N R, Dudley J M, Coen S, Diddams S A, Weber K and Windeler R S 2003Fundamental noise limitations to supercontinuum generation in microstructure fiber *Phys. Rev. Lett.* **90** 113904
[27] Brauckmann N, Kues M, Groß P and Fallnich C 2011 Noise reduction of supercontinua via optical feedback *Opt. Express* **19** 14763–78
[28] Møller U, Sørensen S T, Jakobsen C, Johansen J, Moselund P M, Thomsen C L and Bang O 2012 Power dependence of supercontinuum noise in uniform and tapered PCFs *Opt. Express* **20** 2851–7
[29] Gambetta A, Kumar V, Grancini G, Polli D, Ramponi R, Cerullo G and Marangoni M 2010 Fiber-format stimulated-Raman-scattering microscopy from a single laser oscillator *Opt. Lett.* **35** 226–8
[30] Nose K, Ozeki Y, Kishi T, Sumimura K, Nishizawa N, Fukui K, Kanematsu Y and Itoh K 2012 Sensitivity enhancement of fiber-laser-based stimulated Raman scattering microscopy by collinear balanced detection technique *Opt. Express* **20** 13958–65
[31] Hobbs P C D 1997 Ultrasensitive laser measurements without tears *Appl. Opt.* **36** 903–20
[32] Seto K, Tsukada T, Okuda Y, Tokunaga E and Kobayashi T 2014 Development of a balanced detector with biased synchronous detection and application to near shot noise limited noise cancelling of supercontinuum pulse light *Rev. Sci. Instrum.* **85** 023702
[33] Freudiger C W, Yang W, Holtom G R, Peyghambarian N, Xie X S and Kieu K Q 2014 Stimulated Raman scattering microscopy with a robust fibre laser source *Nature Photon.* **8** 153–9